mater.scichina.com link.springer.com

Published online 28 June 2022 | https://doi.org/10.1007/s40843-022-2082-y
Sci China Mater 2022, 65(11): 2989–2996

High-capacity, high-rate, and dendrite-free lithium metal anodes based on a 3D mixed electronic-ionic conductive and lithiophilic scaffold

Tao Zhang[1], Zhiyuan Sang[1*], Lichang Yin[2], Yonghuan Han[1], Wenping Si[1], Yuxin Yin[3] and Feng Hou[1*]

ABSTRACT **Lithium metal anode possesses a high theoretical capacity and the lowest redox potential, while the severe growth of Li dendrite prevents its practical application. Herein, we prepared a structure of Li_3P nanosheets and Ni nanoparticles decorated on Ni foam (NF) as a three-dimensional (3D) scaffold for dendrite-free Li metal anodes (Li-Li_3P/Ni@Ni foam anodes, shortened as L-LPNNF) using a facile melting method. The Li_3P nanosheets exhibit excellent Li-ion conductivity as well as superior lithiophilicity, and the 3D nickel scaffold provides sufficient electron conductivity and ensures structure stability. Therefore, symmetric cells assembled by L-LPNNF possess lowered voltage hysteresis and improved long cycle stability (a voltage hysteresis of 104.2 mV after 500 cycles at a high current density of 20 mA cm^{-2} with a high capacity of 10 mA h cm^{-2}), compared with the cells assembled with Li foil or Li-NF anodes. Furthermore, the full cells with paired L-LPNNF anodes and commercial $LiFePO_4$ cathodes suggest a specific capacity of 124.6 mA h g^{-1} and capacity retention of 90.8% after 180 cycles with the Coulombic efficiency (CE) of ~100% at a current rate of 1 C. This work provides a potentially scalable option for preparing a mixed electronic-ionic conductive and lithiophilic scaffold for dendrite-free Li anodes at high current densities.**

Keywords: lithium metal anodes, dendrite-free, mixed ionic/electronic conductivity, 3D lithiophilic scaffold

INTRODUCTION

With the rapid development of energy storage equipment, commercialized lithium-ion batteries (LIBs) cannot meet the increasing demand for high energy density in energy storage devices. Lithium metal batteries (LMBs) take advantage of lithium metal's high theoretical capacity (3860 mA h g^{-1}), lowest redox potential (−3.04 V *vs.* H_2/H^+), and low gravimetric density (0.534 g cm^{-3}) to provide high operating voltage and specific storage capacity [1–3]. Beyond LIBs, they are expected to become the next-generation battery system with higher energy density [4]. Nevertheless, due to the high reactivity of lithium metal, LMBs inevitably possess various problems, especially the growth of Li dendrites, hindering their practical application [5]. Nonuniform Li-ion flux and charge allocation aggravate uncontrolled Li deposition, resulting in Li dendrites that can destroy the electrode structure, cause a short circuit, electrolyte consumption, and serious safety accidents.

Several strategies have been adopted to inhibit the growth of Li dendrites, including the use of three-dimensional (3D) scaffold (e.g., a Ni foam (NF) [6–8] and a porous Cu collector [9–11]), the construction of a stable artificial solid electrolyte interphase (SEI) or artificial protective layer (e.g., SrF_2-rich artificial SEI [12], lithium-rich antiperovskites artificial SEI [13], a novel $Li_{6.4}La_3Zr_{1.4}Ta_{0.6}O_{12}$ interface [14] and Li-Sn alloy/Li_3N electrolyte composite interface layer [15]), the optimization of electrolytes (e.g., 1,2-difluorobenzene [16] diluent solvent in the electrolyte, an octaphenyl polyoxyethylene [17] electrolyte additive, and 3D network gel polymer electrolyte [18]). Among them, incorporating a 3D scaffold with lithiophilic sites into the lithium metal matrix is an efficient and facile method for inhibiting the Li dendrites, which can not only effectively reduce the local current density, but also provide a large contact area between the electrolyte and substrates, contributing to uniform Li deposition. Until now, a large number of conversion materials (e.g., Cu_2S [19], ZnO [20], V_2O_5 [21], MoS_2 [22], and AlN [23]) have shown to obtain excellent lithiophilicity *via* chemical reactions with Li. However, these incorporated lithiophilic sites commonly possess intrinsically poor Li-ion conductivity, and the resulting inert Li_2O or Li_2S may be harmful to the transportation of Li-ion flux and results in an uncontrollable dendritic Li formation. As an ideal candidate for modifying 3D scaffolds, Li_3P possesses excellent lithiophilicity and has a low ion and electron transport barrier, facilitating rapid and uniform Li deposition to avoid dendrites. However, the moisture sensitivity of Li_3P makes it unstable in the environment of materials synthesis [24]. Therefore, the *in-situ* conversion reaction of metal phosphide and molten lithium is feasible for preparing Li_3P as reported in recent work [25]. Furthermore, the consistency of the generated Ni metal particles and the introduced 3D NF is beneficial to avoiding the interference of foreign metals on the performance of Li metal anodes.

Herein, we used the *in-situ* conversion reaction between Ni_2P and molten Li to combine the Li_3P and Ni scaffold for dendrite-free Li-Li_3P/Ni@NF anodes (L-LPNNF). *In-situ* Li_3P nanolayers have a good electronic conductivity and high Li^+ conductivity of 10^{-4} S cm^{-1} [25,26], which endow the anode with a mixed electronic-ionic conductive scaffold to ensure the uniform distribution of charge and Li-ion in the subsequent electroplating/

[1] Key Laboratory of Advanced Ceramics and Machining Technology of Ministry of Education, School of Materials Science and Engineering, Tianjin University, Tianjin 300354, China
[2] Shenyang National Laboratory for Materials Science, Institute of Metal Research, Chinese Academy of Sciences, Shenyang 110016, China
[3] Tianjin Lishen Battery Joint Stock Ltd Co, Tianjin 300384, China
[*] Corresponding authors (emails: sangzhiyuan@tju.edu.cn (Sang Z); houf@tju.edu.cn (Hou F))

stripping process. The 3D skeleton of the NF and the generated Ni nanoparticles during the melt impregnation process can withstand the stress and strain caused by the volume change during the electroplating/stripping process, thereby ensuring the stability of the structure. Benefitting from the above advantages, symmetric cells assembled by L-LPNNF suggest a low voltage hysteresis of 104.2 mV after 500 cycles at a high current density of 20 mA cm^{-2} with a high capacity of 10 mA h cm^{-2}. Furthermore, by pairing with commercial $LiFePO_4$ (LFP) cathodes, L-LPNNF|LFP exhibits high-rate performance and long cycle stability at a current rate of 1 C with a specific capacity of 124.6 mA h g^{-1} and capacity retention of 90.8% after 180 cycles, indicating the merits of L-LPNNF for practical applications.

EXPERIMENTAL SECTION

Chemicals and materials

Nickel nitrate hexahydrate ($Ni(NO_3)_2{\cdot}6H_2O$), urea, hydrochloric acid (HCl), acetone, and absolute ethanol were procured from Tianjin Guangfu Chemical Reagent Co., Ltd. Sodium hypophosphite (NaH_2PO_2) was obtained from Shanghai Aladdin Biochemical Technology Co., Ltd. All the chemicals used in the experiments are of analytical grade and were used without further purification. Deionized water was used throughout all the experiments.

Synthesis of L-LPNNF anodes and Li-NF anodes

NF with a thickness of 500 μm, was cut into disks of 12 mm in diameter, ultrasonically pretreated sequentially in acetone and 2 mol L^{-1} HCl solution for 10 min to remove the surface oxide layer and then washed with deionized water and absolute ethanol for three times, respectively. The as-prepared NF was placed in a solution containing 2 mL $Ni(NO_3)_2$ aqueous solution (0.1 mol L^{-1}), 2 mL urea aqueous solution (0.1 mol L^{-1}), and 36 mL deionized water dispersed by ultrasonic for 10 min and then transferred into a Teflon-lined stainless-steel autoclave at 120°C for 8 h. The as-prepared precursor, rinsed with deionized water and naturally dried at room temperature, was placed on one side of a porcelain boat. And NaH_2PO_2, 0.3 times the mass of the as-prepared precursor, was placed on the other side of the porcelain boat. After wrapping the porcelain boat with tinfoil, the NaH_2PO_2 side was placed on the upstream side and heated to 300°C at 2°C min^{-1}. Ni_2P@NFs (NPNF) were obtained after a 2-h reaction and cooled down to room temperature under a flow of Ar atmosphere. The amount of Ni_2P nanosheets grown on NF was about 4.8 mg cm^{-2}, and the mass ratio of Ni_2P nanosheets to NF was about 1:30. L-LPNNF was obtained by placing NPNF in the molten Li metal at 350°C. The same melting process was used for Li-NF anodes (L-NF), except that NFs were used instead of NPNF. To prevent the influence of thickness, Li foils, L-NF, and L-LPNNF were pressed into ~300 μm.

Material characterizations

The microstructures were observed using scanning electron microscopy (SEM, Hitachi, S-4800) at an operating voltage of 5 kV and transmission electron microscopy (TEM, JOEL, JEM-2100) at an acceleration voltage of 200 kV. The crystalline structures were analyzed using X-ray diffraction (XRD, Rigaku D/Max 2500 PC with a Cu Kα radiation λ = 1.54 Å) and X-ray photoelectron spectroscopy (XPS, Kratos Analytical Ltd, Axis Supra $h\nu$ = 15 kV) at room temperature.

Electrochemical tests

The electrolyte was 1.0 mol L^{-1} lithium bis(trifluoromethanesulfonyl) imide (LiTFSI) in a mixture solution of 1,3-dioxolane (DOL) and 1,2-dimethoxyethane (DME) (1:1, vol. ratio) with 1 wt% $LiNO_3$. And 50 μL electrolyte was dropped into each cell, and the polypropylene (PP) membrane (Celgard 2400) was used as the separator. CR2032 coin-type cells were used for electrochemical performance. All cells were assembled in an argon-filled glove box with O_2 and H_2O less than 1.0 ppm (Microuna, China). To test the areal capacity, L-LPNNF were stripped at the current density of 0.25 mA cm^{-2}, where Cu foils were used as counter electrodes. The capacity was calculated before the voltage increase. After stripping at a current density of 0.25 mA cm^{-2}, L-LPNNF are referred to as LPNNF. To test the overpotential, Li|Li, NF|Li, and LPNNF|Li were assembled and platted with 1 mA h cm^{-2} at a current density of 2 mA cm^{-2}. Symmetric cells were assembled using Li|Li, L-NF|L-NF, or L-LPNNF|L-LPNNF to evaluate the long-term cycling stability. The LFP electrodes purchased from MTI Co., Ltd were used as the cathodes for the full-cell tests, with an active mass loading of 120 g m^{-2}, pairing Li, LNF, or LNPNF. The full cells were tested from 2.5 to 4.0 V. A Neware battery testing system was used to measure the electrochemical performance (areal capacity and overpotential) of the symmetric and full cells. The electrochemical impedance spectroscopy (EIS) measurements were performed on a CHI 760E electrochemical workstation with an alternating current (AC) amplitude of 5 mV applied over a frequency range of 100 kHz to 0.01 Hz.

Method of calculation

Density functional theory (DFT) calculations were carried out using the Vienna *ab initio* simulation package (VASP). The calculation adopted the projector augmented-wave (PAW) [27,28] pseudopotentials and Perdew-Burke-Ernzerhof (PBE) generalized gradient approximation functional [29]. The plane-wave energy cutoff was set to 400 eV. The *Γ*-centered *k* mesh density by Monkhorst-Pack method [30] was set to be 0.03 $Å^{-1}$ for all the calculations. The optimization process was repeated until the total energy change of the system was less than 10^{-6} eV, and the atomic position was fully relaxed until the maximum force on each atom was less than −0.01 eV $Å^{-1}$. We used the slab containing 2 × 2 × 1 supercell models with a thickness greater than 10 Å to simulate the anode surfaces, while relaxing the first two layers of Li (1 1 0), Ni (1 1 1), Ni_2P (1 −1 0), and Li_3P (0 0 1). A vacuum space of 15 Å was inserted along the *z*-direction to avoid any interactions between the periodically neighboring structures [31]. The adsorption energies (E_{ads}) of a Li atom on different surfaces were calculated as follows:

$$E_{ads} = E_{Li/slab} - E_{slab} - E_{Li}, \quad (1)$$

where $E_{Li/slab}$, E_{slab}, and E_{Li} are the total energies of different surfaces with a Li atom, different surfaces, and a Li atom, respectively.

RESULTS AND DISCUSSION

As shown in Fig. 1a, the synthetic procedure of L-LPNNF consists of two steps: (1) the preparation of NPNF through a typical hydrothermal-phosphating process from pre-cleaned NF, and (2) the *in-situ* conversion reaction between Ni_2P and Li through a melt impregnation process. After the hydrothermal-phosphating process, Ni_2P nanosheets composed of a pile of rod-

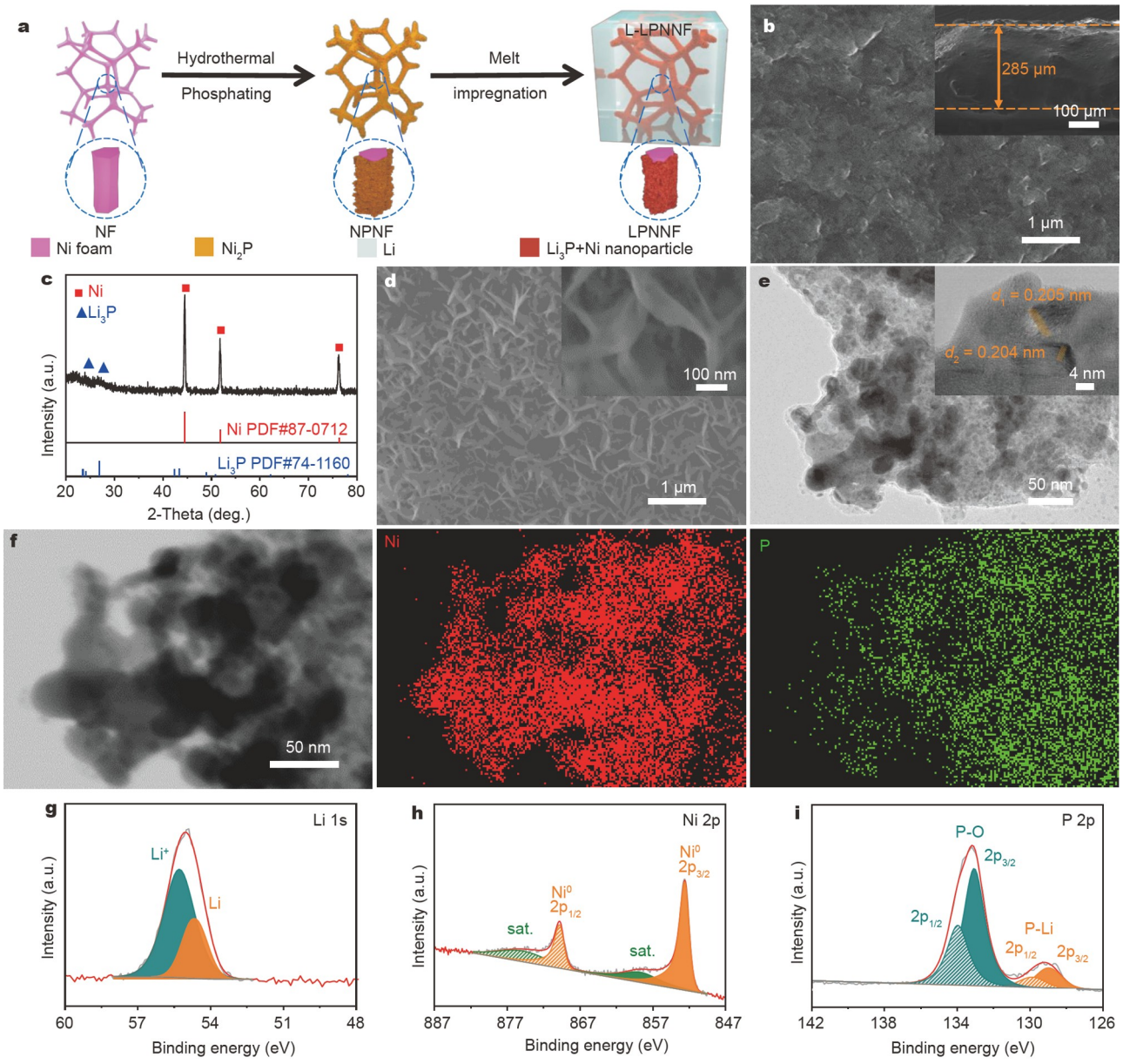

Figure 1 (a) Schematic illustration of the synthetic procedure of L-LPNNF. (b) Front-view SEM image of L-LPNNF. Inset: cross-section SEM image. (c) XRD pattern of LPNNF. (d) SEM images of LPNNF at different magnifications. (e) TEM image of LPNNF. Inset: HRTEM image. (f) EDS mapping images of LPNNF. HRXPS spectrum of LPNNF: (g) Li 1s spectrum, (h) Ni 2p spectrum, and (i) P 2p spectrum.

shaped particles with uniform distribution of Ni and P elements grow on the surface of NF, which is attributed to the decomposition of $Ni(OH)_2$ nanosheets (Figs S1–S3). Then as a comparison, NPNF and NF were used as the skeleton to prepare lithium anodes *via* the melt impregnation process at 350°C. The preparation time of L-LPNNF is about 2 min, which is a quarter of the preparation time of L-NF, indicating that NPNF has a better affinity with molten Li (Videos S1 and S2). The L-LPNNF possesses a surface composed of the finest grains than Li foils and L-NF (Fig. 1b and Fig. S4), which is beneficial for a robust and smooth interfacial layer during electrodeposition [32]. Besides, the thickness of L-LPNNF is 285 μm corresponding to a specific areal capacity of 63.2 mA h cm^{-2} (Fig. S5, corresponding Li amounts: 16.4 mg cm^{-2}), which is greater than that of L-NF (Fig. S6, 273 μm, 59.1 mA h cm^{-2}) and closer to that of Li (Fig. S7, 290 μm), indicating the better Li loading capacity of NPNF than NF.

In order to understand the changes in the surface of the scaffold, lithium metal was removed from L-LPNNF by stripping at the current density of 0.25 mA cm^{-2} (named LPNNF). Besides the obvious Ni peak, the peaks at 23.4° and 26.8° correspond to the (002) and (101) crystal facets of PDF#87-0712 Li_3P, respectively (Fig. 1c). The Li_3P/Ni suggests a nanosheet structure on the surface of NF (Fig. 1d). The high-resolution TEM (HRTEM) image (Fig. 1e) shows Ni metal nanoparticles (d_1 = 0.205 nm, d_2 = 0.204 nm, Fig. S8) corresponding to Ni (1 1 1) crystal facet are distributed in LPNNF, which helps the occurrence of the conversion reaction of Ni_2P and Li. Energy dispersive X-ray spectroscopy (EDS) mapping images further suggest the distributions of Ni and P elements are inconsistent across the

LPNNF nanosheets (Fig. 1f). In the HRXPS spectrum of Li 1s for LPNNF, two peaks at 55.3 and 54.6 eV indicate the existence of Li^+ and Li metal (Fig. 1g), and the Li^+ peak may be induced by the existence of Li_3P [33]. In the high-resolution Ni 2p spectrum of LPNNF, there are two sharp peaks at 852.6 and 869.9 eV that correspond to Ni $2p_{3/2}$ and Ni $2p_{1/2}$ of Ni^0, respectively [34], instead of $Ni^{\delta+}$ of Ni–P and Ni–P–O in NPNF [35–37], indicating the disappearance of Ni_2P and further illustrating the complete conversion of Ni_2P to Li_3P (Fig. 1h, Fig. S3e). In the P 2p spectrum, the changes from the Ni–P bond at 129.5 eV (P $2p_{3/2}$) and 130.4 eV (P $2p_{1/2}$) to two peaks at 129.0 eV (P $2p_{3/2}$) and 130.0 eV (P $2p_{1/2}$) of the Li–P bond also indicate the existence of the conversion reaction between Ni_2P and Li (Fig. 1i, Fig. S3f) [26,38,39]. Another two peaks at 134.0 and 133.1 eV are assigned to the P–O bond due to the oxidation of surface P on metal phosphide by air [40]. As a result of the abundant contact surfaces and the *in-situ* chemical reaction, Ni_2P nanosheets can improve the wettability of NF and lithium metal. Furthermore, the Li_3P formed on the surface of scaffolds during the melt impregnation process is a key factor determining the subsequent electroplating/stripping.

To clarify the lithiophilicity during the electroplating process, the nucleation overpotentials of three different types of anodes were characterized. In addition to its excellent affinity for Li, LPNNF exhibits a 22.6 mV nucleation overpotential at a deposition current density of 2 mA cm^{-2}, indicating that it has the lowest Li-ion nucleation barrier among the three candidates (Fig. 2a). We further analyzed the reaction kinetics by EIS to study the Li-ion conductivity of LPNNF. For fresh symmetric cells, the resistance of charge transport at the interface (R_{ct} = 90.1 Ω) and the resistance between electrolyte and electrode (R_Ω = 3.2 Ω) of L-LPNNF|L-LPNNF are significantly lower than that of Li and L-NF, indicating the lowest charge transport barrier of the surface passivation layer and better connection between the electrolyte and electrode (Fig. 2b). Furthermore, in the low-frequency region, the Warburg factor (δ) can be obtained using the slope of the fitting curve referring to real parts of the impedance (Z') and the reciprocal square root of the angular frequency (ω), which has the relationship with Li-ion diffusion efficiency (D_{Li}), as shown in Equation (2):

$$D_{Li} = \frac{R^2T^2}{2A^2n^4F^4C^2\delta^2}, \quad (2)$$

where R is the gas constant, T is the absolute temperature, A is the surface area of the electrode, n is the number of electrons per molecule during oxidization, F is the Faraday constant, and C is the concentration of the Li-ion. The smallest δ value for L-LPNNF reflects the fastest Li-ion diffusion process compared with Li and L-NF (Fig. 2c).

To have a deeper understanding of the chemical affinity between scaffolds and Li, we used DFT to calculate the adsorption energies of the Li atom on the surface of different materials. The optimized adsorption structures with a single Li on the Li (1 1 0), Ni (1 1 1), and Li_3P (0 0 1), which are the lowest energy surfaces for individual compositions by calculation, are illustrated in Fig. S9. For Li_3P, the strong adsorption energy of −3.348 eV ensures that Li_3P has perfect lithiophilicity during the subsequent electroplating/stripping process (Fig. 2d). The net charge loss above the Li atom and the net charge gain on the adjacent surfaces from the charge density difference isosurfaces of Li (1 1 0), Ni (1 1 1), and Li_3P (0 0 1) (Fig. S10 and Fig. 2e, f) confirm that the charge transfer between Li and Li/P atoms is the strongest among these three surfaces, indicating the strongest interaction between Li and Li_3P (0 0 1). Furthermore,

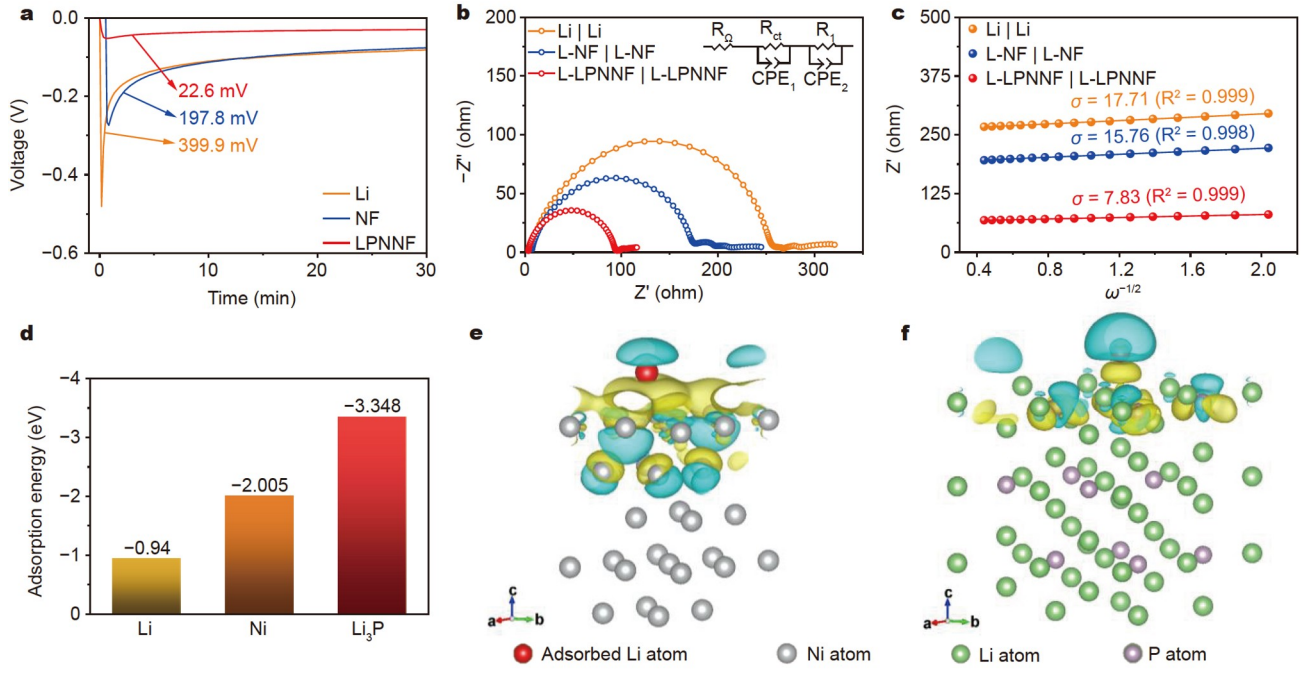

Figure 2 (a) The voltage profiles of Li deposition on Li, NF, and LPNNF. (b) Nyquist plots of fresh Li|Li, L-NF|L-NF, and L-LPNNF|L-LPNNF symmetric cells. (c) The relationship between real parts of the impedance (Z') and the reciprocal square root of the angular frequency (ω) in the low-frequency region for Li|Li, L-NF|L-NF, and L-LPNNF|L-LPNNF symmetric cells. (d) The adsorption energy of a Li atom with different surfaces. Charge density difference isosurfaces with a single Li on the (e) Ni (1 1 1), and (f) Li_3P (0 0 1) surfaces, respectively. 0.0015 e $Bohr^{-3}$. Cyan: −, yellow: +, red: an adsorbed Li atom, silvery: Ni atoms, green: Li atoms, purple: P atoms.

when compared with $Li_2O/Li_2S/Li_3N$, oxides/sulfides/nitrides will inevitably form lithiophilic sites, the difference between the highest occupied molecular orbital (HOMO) and lowest unoccupied molecular orbital (LUMO) orbitals of Li_3P is only 0.84 eV, indicating that it has more excellent electronic conductivity (Fig. S11). Meanwhile, the high electrical conductivity and nanoscale distribution of Ni metal nanoparticles help to reduce the local current density and maintain structural stability. The perfect lithiophilicity and excellent mixed electron-ion conductivity of L-LPNNF ensure the uniform distribution of charges and Li-ions in the subsequent electroplating/stripping process, thereby alleviating the hysteresis problem and inhibiting dendrite growth during deposition.

The cycling stability and reversibility of Li, L-NF, and L-LPNNF symmetric cells were evaluated through the electroplating/stripping process. Compared with Li|Li and L-NF|L-NF, L-LPNNF|L-LPNNF has a more stable cycling performance and smaller voltage hysteresis. After cycling for 500 h, the symmetrical cell based on L-LPNNF retains a low voltage hysteresis of 10.1 mV with a stable and smooth profile from the electroplating/stripping process with the capacity of 1 mA h cm^{-2} at a current density of 2 mA cm^{-2} (Fig. 3a). However, Li|Li and L-NF|L-NF possess much higher voltage hysteresis of 72.1 and 57.7 mV at the beginning of the repeated electroplating/stripping process, which gradually increase to 258.1 and 231.3 mV at 500 h, respectively. Furthermore, we also examined the EIS data of the symmetric batteries after 200 cycles (Fig. S12). Nyquist plots present a small semicircle diameter and large slope of L-LPNNF|L-LPNNF, indicating the excellent charge carrier transportability and stable properties of L-LPNNF. When increasing the current density to 5 mA cm^{-2} and the electroplating/stripping capacity to 2.5 mA h cm^{-2}, L-LPNNF|L-

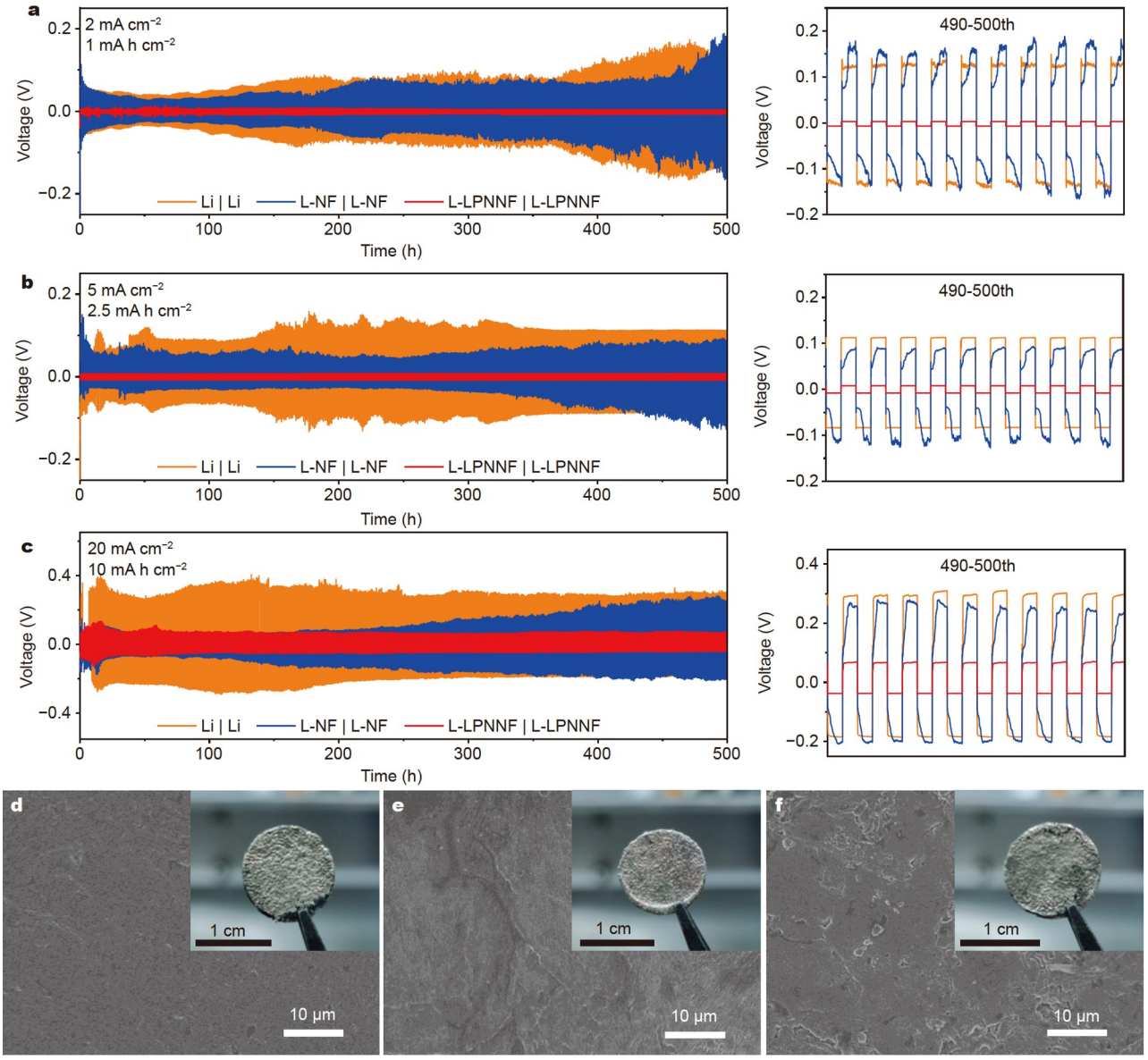

Figure 3 Electrochemical performances of the symmetric cells and comparison of voltage hysteresis of Li electroplating/stripping at various current densities and fixed areal capacity: (a) 1 mA h cm^{-2} at 2 mA cm^{-2}, (b) 2.5 mA h cm^{-2} at 5 mA cm^{-2}, (c) 10 mA h cm^{-2} at 20 mA cm^{-2}. SEM images of L-LPNNF|L-LPNNF after 500 cycling at various current densities and fixed areal capacity: (d) 1 mA h cm^{-2} at 2 mA cm^{-2}, (e) 2.5 mA h cm^{-2} at 5 mA cm^{-2}, (f) 10 mA h cm^{-2} at 20 mA cm^{-2}.

LPNNF exhibits a lifespan up to 500 h with the voltage hysteresis of 15.7 mV (Fig. 3b), much lower than that of Li|Li (195.6 mV) and L-NF|L-NF (173.3 mV). Even at 20 mA cm^{-2}, L-LPNNF|L-LPNNF achieves stable cycling of electroplating-stripping for 500 h without a short circuit at a high areal capacity of 10 mA h cm^{-2}, verifying the merits of L-LPNNF for rapid and deep Li deposition (Fig. 3c). The voltage profiles at a current density of 2 mA cm^{-2} present that LPNNF has a 15.2 mV nucleation overpotential lower than that of Li and NF after 500 cycles, indicating that the surface Li_3P is not covered by dead Li (Fig. S13). From the initial and following cycles (Fig. S14), the similar transitions from "peak" to "arc" and then to "plateau" with increasing voltage hysteresis in the voltage profiles of Li|Li, and L-NF|L-NF indicate the accumulation of dead Li and electrolyte depletion [41,42]. For L-LPNNF|L-LPNNF, the Li_3P nanolayers and Ni metal nanoparticles with well ionic and electronic conductivity guarantee the uniform lithium deposition, ensuring the "plateau" voltage profiles with constant voltage hysteresis. Thus, L-LPNNF|L-LPNNF suggests an improved performance, significantly better than the recently published symmetrical cells (Table S1).

We also characterized the surface morphologies of the L-LPNNF after cycling at different current densities and compared them with pure Li and L-NF anodes. It can be seen that regardless of the conditions under which the electroplating/stripping process is carried out, the surface of pure Li foils changes from a dense to a loose structure (Fig. S15). For L-NF, the porosity of anodes decreases after cycling (Fig. S16). For L-LPNNF, the surfaces are still flat after 500 h cycling with a 0.5-h electroplating/stripping process at a current density of 2, 5, 20 mA cm^{-2}, respectively (Fig. 3d–f).

Full cells were assembled to verify the practicality of the anodes by pairing L-LPNNF with commercial LFP cathodes. Compared with Li|LFP and L-NF|LFP, L-LPNNF|LFP has better rate capability and longer cycling performance. Specifically, L-LPNNF|LFP has a reversible capacity of 100 mA h g^{-1} at a high current density of 3 C. When the current density returns to 0.5 C, the specific capacity of L-LPNNF|LFP still retains 141 mA h g^{-1}, showing its high reversibility of L-LPNNF (Fig. 4a). As shown in Fig. 4b, L-LPNNF|LFP delivers a polarization of 146, 236, 410, 605, 430, 244, and 144 mV at the rates of 0.5, 1, 2, 3, 2, 1, and 0.5 C, respectively, which are lower than that of Li|LFP, and L-NF|LFP (Fig. 4c and Fig. S17), indicating excellent reaction kinetics of L-LPNNF at various rates. From the cycling performance at a current rate of 1 C (Fig. 4d, e), L-LPNNF|LFP has a specific capacity of 124.6 mA h g^{-1} and capacity retention of 90.8% after 180 cycles. And the Coulombic efficiency (CE) of L-LPNNF|LFP is always around 100%, whereas the CE of Li|LFP and L-NF|LFP both drop rapidly at 90 and 157 cycles (Fig. S18). And the capacity fluctuations originated from uncontrolled temperature changes during testing. To clear the effect of temperature on the capacity, we tested Li|LFP and L-LPNNF|LFP full cells at different temperatures (22 and 29°C). Significantly, the specific capacity increment of L-LPNNF|LFP is less affected by temperature (1.94 mA h g^{-1} °C^{-1}, Fig. S19) than that of Li|LFP (2.51 mA h g^{-1} °C^{-1}, Fig. S20) in the range of 22 to 29°C. This result indicates that the full cells with L-LPNNF can maintain stable charge-discharge performance under temperature fluctuations. To meet practical requirements, we thinned L-LPNNF to 94 μm, corresponding to a specific areal capacity of 9 mA h cm^{-2} (Fig. S21, named as L-LPNNF (thin)). As shown in Fig. S22, the L-LPNNF (thin)|LFP with limited electrolyte (20 μL) still suggests a large reversible capacity (~150 mA h g^{-1} with respect to the mass of LFP) and good stability. Meanwhile, the increased Li utilization in the L-LPNNF|LFP suggests that L-LPNNF has the potential for practical applications.

CONCLUSION

In this work, we prepared L-LPNNF anodes with a unique

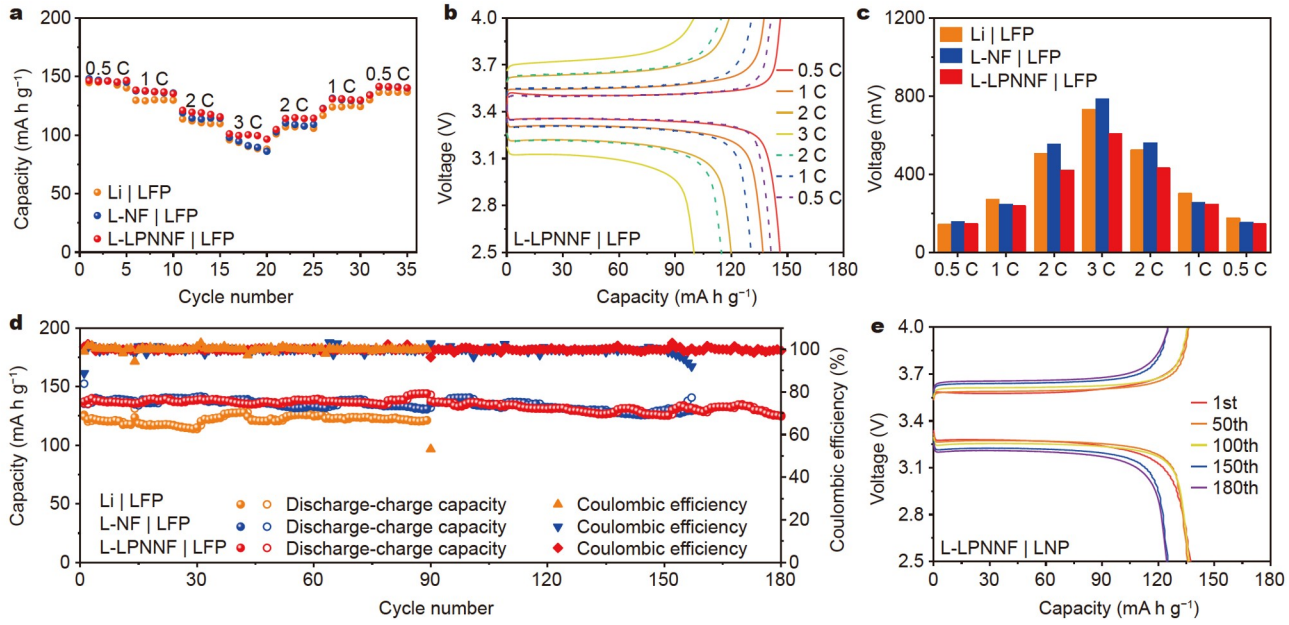

Figure 4 (a) Rate performances of full cells. (b) Voltage profiles of LNPNF|LFP at different current rates from 0.5 to 3 C then back to 0.5 C (1 C = 170 mA g^{-1}). (c) The comparison of voltage hysteresis of Li|LFP, L-NF|LFP, and L-LPNNF|LFP. (d) Cycling performances of full cells at 1 C. (e) Voltage profiles of L-LPNNF|LFP at 1 C.

structure of Li_3P layer and Ni nanoparticles generated by the *in-situ* conversion reaction between Ni_2P and molten Li. Due to the perfect lithiophilicity and ionic-electron mixed conductivity, the Li-ion nucleation process can be guided, resulting in a stable reversible electroplating/stripping process and a long lifespan of L-LPNNF. As a result, L-LPNNF symmetric cells can maintain stable voltage hysteresis at various current densities and capacities, ensuring the merits of L-LPNNF for full cells and supporting the potential for practical applications. Furthermore, this research clarifies that the Li_3P layer is vital to dendrite-free Li anodes, and provides a scalable surface control method with application potential.

Received 30 January 2022; accepted 15 April 2022; published online 28 June 2022

1 Zhang X, Wang A, Liu X, *et al.* Dendrites in lithium metal anodes: Suppression, regulation, and elimination. Acc Chem Res, 2019, 52: 3223–3232
2 Zheng J, Kim MS, Tu Z, *et al.* Regulating electrodeposition morphology of lithium: Towards commercially relevant secondary Li metal batteries. Chem Soc Rev, 2020, 49: 2701–2750
3 Wu H, Zhang Y, Deng Y, *et al.* A lightweight carbon nanofiber-based 3D structured matrix with high nitrogen-doping level for lithium metal anodes. Sci China Mater, 2019, 62: 87–94
4 Cheng XB, Zhang R, Zhao CZ, *et al.* Toward safe lithium metal anode in rechargeable batteries: A review. Chem Rev, 2017, 117: 10403–10473
5 Shen L, Shi P, Hao X, *et al.* Progress on lithium dendrite suppression strategies from the interior to exterior by hierarchical structure designs. Small, 2020, 16: 2000699
6 Chi SS, Liu Y, Song WL, *et al.* Prestoring lithium into stable 3D nickel foam host as dendrite-free lithium metal anode. Adv Funct Mater, 2017, 27: 1700348
7 Yue XY, Wang WW, Wang QC, *et al.* CoO nanofiber decorated nickel foams as lithium dendrite suppressing host skeletons for high energy lithium metal batteries. Energy Storage Mater, 2018, 14: 335–344
8 Pei F, Fu A, Ye W, *et al.* Robust lithium metal anodes realized by lithiophilic 3D porous current collectors for constructing high-energy lithium-sulfur batteries. ACS Nano, 2019, 13: 8337–8346
9 Lin K, Xu X, Qin X, *et al.* Restructured rimous copper foam as robust lithium host. Energy Storage Mater, 2020, 26: 250–259
10 Qian J, Wang S, Li Y, *et al.* Lithium induced nano-sized copper with exposed lithiophilic surfaces to achieve dense lithium deposition for lithium metal anode. Adv Funct Mater, 2021, 31: 2006950
11 Yun Q, He YB, Lv W, *et al.* Chemical dealloying derived 3D porous current collector for Li metal anodes. Adv Mater, 2016, 28: 6932–6939
12 Liu S, Ji X, Yue J, *et al.* High interfacial-energy interphase promoting safe lithium metal batteries. J Am Chem Soc, 2020, 142: 2438–2447
13 Han B, Feng D, Li S, *et al.* Self-regulated phenomenon of inorganic artificial solid electrolyte interphase for lithium metal batteries. Nano Lett, 2020, 20: 4029–4037
14 Shi K, Wan Z, Yang L, *et al.* *In situ* construction of an ultra-stable conductive composite interface for high-voltage all-solid-state lithium metal batteries. Angew Chem Int Ed, 2020, 59: 11784–11788
15 Yu J, Shi K, Zhang S, *et al.* A lithium nucleation-diffusion-growth mechanism to govern the horizontal deposition of lithium metal anode. Sci China Mater, 2021, 64: 2409–2420
16 Yoo DJ, Yang S, Kim KJ, *et al.* Fluorinated aromatic diluent for high-performance lithium metal batteries. Angew Chem Int Ed, 2020, 59: 14869–14876
17 Dai H, Gu X, Dong J, *et al.* Stabilizing lithium metal anode by octaphenyl polyoxyethylene-lithium complexation. Nat Commun, 2020, 11: 643
18 Lu Q, He YB, Yu Q, *et al.* Dendrite-free, high-rate, long-life lithium metal batteries with a 3D cross-linked network polymer electrolyte. Adv Mater, 2017, 29: 1604460
19 He D, Liao Y, Cheng Z, *et al.* Facile one-step vulcanization of copper foil towards stable Li metal anode. Sci China Mater, 2020, 63: 1663–1671
20 Yue XY, Bao J, Yang SY, *et al.* Petaloid-shaped ZnO coated carbon felt as a controllable host to construct hierarchical Li composite anode. Nano Energy, 2020, 71: 104614
21 Huang G, Guo P, Wang J, *et al.* Lithiophilic V_2O_5 nanobelt arrays decorated 3D framework hosts for highly stable composite lithium metal anodes. Chem Eng J, 2020, 384: 123313
22 Yuan H, Nai J, Fang Y, *et al.* Double-shelled C@MoS_2 structures preloaded with sulfur: An additive reservoir for stable lithium metal anodes. Angew Chem Int Ed, 2020, 59: 15839–15843
23 Zhang T, Lu H, Yang J, *et al.* Stable lithium metal anode enabled by a lithiophilic and electron/ion conductive framework. ACS Nano, 2020, 14: 5618–5627
24 Mao E, Wang W, Wan M, *et al.* Confining ultrafine Li_3P nanoclusters in porous carbon for high-performance lithium-ion battery anode. Nano Res, 2020, 13: 1122–1126
25 Sun C, Lin A, Li W, *et al.* *In situ* conversion of Cu_3P nanowires to mixed ion/electron-conducting skeleton for homogeneous lithium deposition. Adv Energy Mater, 2020, 10: 1902989
26 Zhang C, Lyu R, Lv W, *et al.* A lightweight 3D Cu nanowire network with phosphidation gradient as current collector for high-density nucleation and stable deposition of lithium. Adv Mater, 2019, 31: 1904991
27 Kresse G, Furthmüller J. Efficiency of *ab-initio* total energy calculations for metals and semiconductors using a plane-wave basis set. Comput Mater Sci, 1996, 6: 15–50
28 Kresse G, Furthmüller J. Efficient iterative schemes for *ab initio* total-energy calculations using a plane-wave basis set. Phys Rev B, 1996, 54: 11169–11186
29 Perdew JP, Burke K, Ernzerhof M. Generalized gradient approximation made simple. Phys Rev Lett, 1996, 77: 3865–3868
30 Monkhorst HJ, Pack JD. Special points for Brillouin-zone integrations. Phys Rev B, 1976, 13: 5188–5192
31 Sa B, Li YL, Qi J, *et al.* Strain engineering for phosphorene: The potential application as a photocatalyst. J Phys Chem C, 2014, 118: 26560–26568
32 Dong J, Dai H, Fan Q, *et al.* Grain refining mechanisms: Initial levelling stage during nucleation for high-stability lithium anodes. Nano Energy, 2019, 66: 104128
33 Lin L, Liang F, Zhang K, *et al.* Lithium phosphide/lithium chloride coating on lithium for advanced lithium metal anode. J Mater Chem A, 2018, 6: 15859–15867
34 Tanaka A, Teramura K, Hosokawa S, *et al.* Visible light-induced water splitting in an aqueous suspension of a plasmonic Au/TiO_2 photocatalyst with metal co-catalysts. Chem Sci, 2017, 8: 2574–2580
35 Pan Y, Liu Y, Zhao J, *et al.* Monodispersed nickel phosphide nanocrystals with different phases: Synthesis, characterization and electrocatalytic properties for hydrogen evolution. J Mater Chem A, 2015, 3: 1656–1665
36 Bernasconi R, Khalil MI, Iaquinta C, *et al.* Nickel phosphides fabricated through a codeposition-annealing technique as low-cost electrocatalytic layers for efficient hydrogen evolution reaction. ACS Appl Energy Mater, 2020, 3: 6525–6535
37 Lu X, Baker MA, Anjum DH, *et al.* Ni_2P nanoparticles embedded in mesoporous SiO_2 for catalytic hydrogenation of SO_2 to elemental S. ACS Appl Nano Mater, 2021, 4: 5665–5676
38 Du Z, Ai W, Yang J, *et al.* *In situ* fabrication of Ni_2P nanoparticles embedded in nitrogen and phosphorus codoped carbon nanofibers as a superior anode for Li-ion batteries. ACS Sustain Chem Eng, 2018, 6: 14795–14801
39 Yang J, Yang N, Xu Q, *et al.* Bioinspired controlled synthesis of NiSe/Ni_2P nanoparticles decorated 3D porous carbon for Li/Na ion batteries. ACS Sustain Chem Eng, 2019, 7: 13217–13225
40 Yu XY, Feng Y, Guan B, *et al.* Carbon coated porous nickel phosphides nanoplates for highly efficient oxygen evolution reaction. Energy Environ Sci, 2016, 9: 1246–1250
41 Wood KN, Kazyak E, Chadwick AF, *et al.* Dendrites and pits: Untangling the complex behavior of lithium metal anodes through operando video microscopy. ACS Cent Sci, 2016, 2: 790–801

42 Chen KH, Wood KN, Kazyak E, *et al.* Dead lithium: Mass transport effects on voltage, capacity, and failure of lithium metal anodes. J Mater Chem A, 2017, 5: 11671–11681

Acknowledgements This work was financially supported by the National Natural Science Foundation of China (51072130, 51502045 and 21905202).

Author contributions Si W and Hou F conceived the project. Zhang T designed and engineered the samples; Yin L, Han Y, and Yin Y helped with the characterization. Zhang T wrote the paper with support from Sang Z and Hou F. All authors contributed to the general discussion.

Conflict of interest The authors declare that they have no conflict of interest.

Supplementary information Supporting data are available in the online version of the paper.

Tao Zhang received his BSc degree from the Advanced Ceramics Institute at Tianjin University in 2018 and continued his study as a master's candidate under the guidance of Associate Professor Feng Hou till 2021. His research interest mainly focuses on the design and preparation of lithium metal anodes.

Zhiyuan Sang received his PhD degree from Tianjin University in 2020. He is now working as a postdoctoral research fellow at Tianjin University. His research interest mainly focuses on electrochemical energy storage and conversion.

Feng Hou received his PhD degree from the Advanced Ceramics Institute at Tianjin University in 2001 and is now an associate professor at the School of Materials Science and Engineering, Tianjin University. His research interests focus on electrochemical energy storage and conversion.

基于三维电子离子共导亲锂骨架的高容量、高倍率和无枝晶锂金属负极

张涛[1], 桑志远[1*], 尹利长[2], 韩永欢[1], 司文平[1], 阴育新[3], 侯峰[1*]

摘要 锂金属负极因具有较高的理论容量和最低的氧化还原电位有望成为下一代电池负极材料, 而严重的锂枝晶生长阻碍了其实际应用. 本文中, 我们制备了Li_3P纳米片和Ni纳米颗粒修饰的泡沫镍结构作为无枝晶锂金属负极的三维骨架. 其中Li_3P纳米片表现出优异的锂离子电导率和优异的亲锂性, 三维镍骨架可提供足够的电子电导率并确保结构稳定性. 由该负极组装的对称电池具有低电压滞后和长循环稳定性(在20 mA cm^{-2}和10 mA h cm^{-2}下电镀/剥离循环500次后的电压滞后为104.2 mV). 同时, 由该负极和商用$LiFePO_4$正极配对的全电池具有较好的循环稳定性(180次循环后的比容量为124.6 mA h g^{-1}, 对应容量保持率为90.8%). 这种方法制备的三维电子离子共导亲锂骨架为高电流密度下无枝晶锂负极提供了一种潜在的可扩展选择.

